nature materials

Article

https://doi.org/10.1038/s41563-026-02775-4

Direct imaging elucidates ionic memory in two-dimensional nanochannels

Received: 2 December 2025

Accepted: 18 September 2026

Published online: 27 October 2026

Check for updates

Kalluvadi Veetil Saurav[1,2,10], Nathan Ronceray[3,9,10], Baptiste Coquinot[4], Agustin D. Pizarro[3], Ashok Keerthi[1,2,5], Theo Emmerich[3,6] ✉, Aleksandra Radenovic[3,7] ✉ & Boya Radha[2,5,8] ✉

Nanofluidic memristors promise brain-inspired information processing with ions, yet their microscopic origin remains debated. So far, ionic memory has been attributed to ion-specific interactions, dynamic wetting, chemical reactions or mechanical deformations, yet typically without direct experimental evidence. Here, by combining operando interferometric imaging with electrokinetic measurements, we directly visualize voltage-induced blistering of the confining walls of two-dimensional (2D) nanochannels as the key origin of memristive hysteresis. We identify two distinct classes of blisters: unidirectional, driven by electrostatic forces on surface charges, and bidirectional, arising from osmotic pressure due to concentration polarization. This mechanistic framework explains device evolution and device-to-device variability, and reframes stochastic blistering as a functional design element. Our results constitute a direct proof of electromechanical coupling as a robust pathway to ionic memory in 2D nanochannels and open routes towards high-performance ionic memristors and electrically actuated nanofluidic valves.

Emerging phenomena in nanoscale ion transport under extreme confinement are a major interest of nanofluidics[1,2], both for the fundamental questions they raise and for their potential to enable novel applications. In particular, striking nonlinearities such as hyperbolic currents[3], diode-like rectification[4–8] and memristive hysteresis[9–14] have been experimentally observed in a variety of nanofluidic devices. Memristive nanofluidic devices have attracted significant attention by enabling neuromorphic nanofluidics, a new field aiming at processing information with solvated ions, thereby mimicking the brain[15–17]. In most studies, the physical origin of nonlinear ion transport is rationalized either through molecular simulations or through phenomenological models involving ad hoc new physics in extreme confinement. By relying on idealized devices, these approaches often fail to capture the experimentally observed devices' stochasticity and evolution, which is a major obstacle towards the realization of reliable nanopore-based technologies[18–20]. Thus, operando imaging approaches are much needed to complement 'blind' electrokinetic measurements and uncover unambiguously the mechanisms of nanoscale ion transport.

A recent study combined optical and electrokinetic measurements to reveal the origin of ionic memory in highly asymmetric channels, showing that voltage-induced mechanical deformations modulate confinement and, consequently, device conductance[21]. However, the working principle of many other nanofluidic memristors remains an open question. In two-dimensional (2D) nanochannels made by van der Waals assembly for instance, it has been hypothesized that ion-specific effects such as ionic pairing and polyelectrolyte formation were at the

[1]Department of Chemistry, School of Natural Sciences, The University of Manchester, Manchester, UK. [2]National Graphene Institute, The University of Manchester, Manchester, UK. [3]Institute of Bioengineering, School of Engineering, EPFL, Lausanne, Switzerland. [4]Institute of Science and Technology Austria (ISTA), Klosterneuburg, Austria. [5]Photon Science Institute, The University of Manchester, Manchester, UK. [6]Laboratoire de Physique, UMR CNRS 5672, ENS de Lyon, Université de Lyon, Lyon, France. [7]NCCR Bio-Inspired Materials, EPFL, Lausanne, Switzerland. [8]Department of Physics and Astronomy, School of Natural Sciences, The University of Manchester, Manchester, UK. [9]Present address: Laboratoire Photonique Numérique et Nanosciences, Institut d'Optique Graduate School, CNRS UMR 5298, Université de Bordeaux, Talence, France. [10]These authors contributed equally: Kalluvadi Veetil Saurav, Nathan Ronceray. ✉e-mail: theo.emmerich@ens-lyon.fr; aleksandra.radenovic@epfl.ch; radha.boya@manchester.ac.uk

https://doi.org/10.1038/s41563-026-02775-4

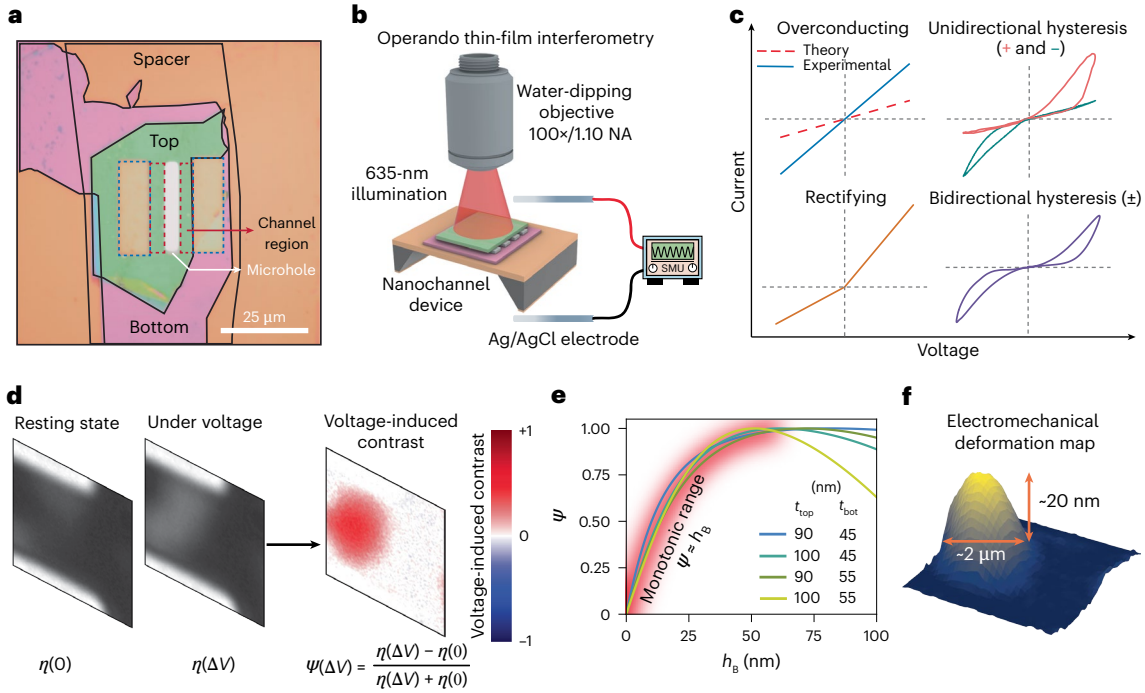


Fig. 1 | Operando microscopy of a 2D nanochannel device and methodology. **a**, Optical image of device 2 (two-layer graphene spacer) depicting the trilayer stack of hBN–graphene–hBN on SiN_x membrane with a ~3-µm × 25-µm microhole and rectangular aperture separated from the microhole by a fixed length defined as L. **b**, Schematic of operando measurement set-up wherein a water-dipping objective is used to visualize the device dynamics while simultaneously recording the ionic current. NA, numerical aperture. **c**, Representative I–V characteristics, namely overconducting (the dashed line represents the theoretical current value), rectifying and two types of memristor (unidirectional hysteresis and bidirectional hysteresis), as observed and discussed in the text. **d**, Image processing methodology for the quantification of voltage-induced blisters from raw reflectance images. The VIC $\Psi(\Delta V)$ is evaluated as the Michelson contrast of the raw intensity images at rest $\eta(0)$ and under an applied voltage $\eta(\Delta V)$. **e**, Contrast–height curves $\Psi(h_B)$ for various t_{top} and t_{bot} used in this study. The highlighted red region shows the range of monotonic scaling between $\Psi(h_B)$ and h_B. **f**, Blister topography extracted from **d** and **e** with typical values of blister height and diameter.

root of ionic memory[13,22–24]. However, a direct experimental proof is still lacking. Here, we combine optical thin-film interferometry and electrokinetic measurements to directly observe the phenomenon triggering memristive hysteresis in 2D nanochannels. We observe that voltage-induced mechanical deformations lead to nonlinear ion transport in 2D channels. We further identify the electromechanical effects that explain these deformations through systematic characterization and analytical modelling.

Design and correlative measurements of 2D nanochannels

For the fabrication of 2D nanochannel devices, a modified version of the fabrication process (Supplementary Fig. 1) previously reported was followed[25,26], wherein a bottom hexagonal boron nitride (hBN) flake is transferred onto a silicon nitride (SiN_x) free-standing membrane with a ~3-µm × 25-µm microhole. A few-layer graphene flake patterned using electron-beam lithography and dry etching serves as a spacer layer. Supplementary Fig. 1c shows an atomic force microscopy image of the spacer. A top hBN flake completes the trilayer stack, into which a rectangular aperture is dry etched to define the channel length, $L \approx 5$ µm. Importantly, the top and bottom thicknesses t_{top} and t_{bot} change not only the mechanical but also the optical properties of the devices and had to be chosen carefully. The full details of the $N = 14$ devices measured in this study are provided in Supplementary Table 1.

Our measurement set-up consists of a custom fluidic cell with a top reservoir large enough to fit a water-dipping objective (Fig. 1b). The device is observed via wide-field reflection imaging with quasi-monochromatic normal-incidence illumination enabling the quantification of the device topography by using thin-film interferometry[21,27]. Ion transport is induced by applying a sinusoidal potential drop $\Delta V(t) = \Delta V_0 \sin(2\pi f t)$ with varying amplitude ΔV_0 and frequency f across Ag/AgCl electrodes connected to a digital–analogue converter for recording. The camera is triggered with the digital–analogue converter to synchronize optical and electrokinetic data (Supplementary Fig. 2). In this study, we used aqueous solutions of KCl in various concentrations from 1 mM to 1 M as well as 1-M solutions of NaCl, LiCl and $CaCl_2$ (Supplementary Fig. 6). Our coupled electrokinetic–optical investigation is motivated by the striking diversity of current–voltage characteristics previously reported in nominally identical 2D nanochannels[13,28,29]. As illustrated in Fig. 1c, these include linear but overconducting traces, strongly rectifying behaviours, and unidirectional or bidirectional memristive hysteresis. Such variability is difficult to reconcile with purely electrokinetic models, leading us to hypothesize that it instead originates from voltage-induced mechanical deformations that are naturally diverse in their manifestation[21].

Quantifying nanoscale deformations via image voltage-induced contrast (VIC)

We found that the application of a voltage resulted in visible features, namely liquid-filled blisters of nanoscale height h_B and microscale lateral extension. In this work, we introduce a methodology for the quantification of the voltage-induced deformations of the device (Fig. 1d) through the VIC $\Psi(\Delta V)$, defined for each pixel as

$$\Psi(\Delta V) = \frac{\eta(\Delta V) - \eta(0)}{\eta(\Delta V) + \eta(0)} \quad (1)$$

where $\eta(\Delta V)$ is the intensity value for an applied voltage ΔV. This metric can be understood as the voltage-induced Michelson contrast and has values between −1 and +1. It depends on the thickness of all the layers

https://doi.org/10.1038/s41563-026-02775-4

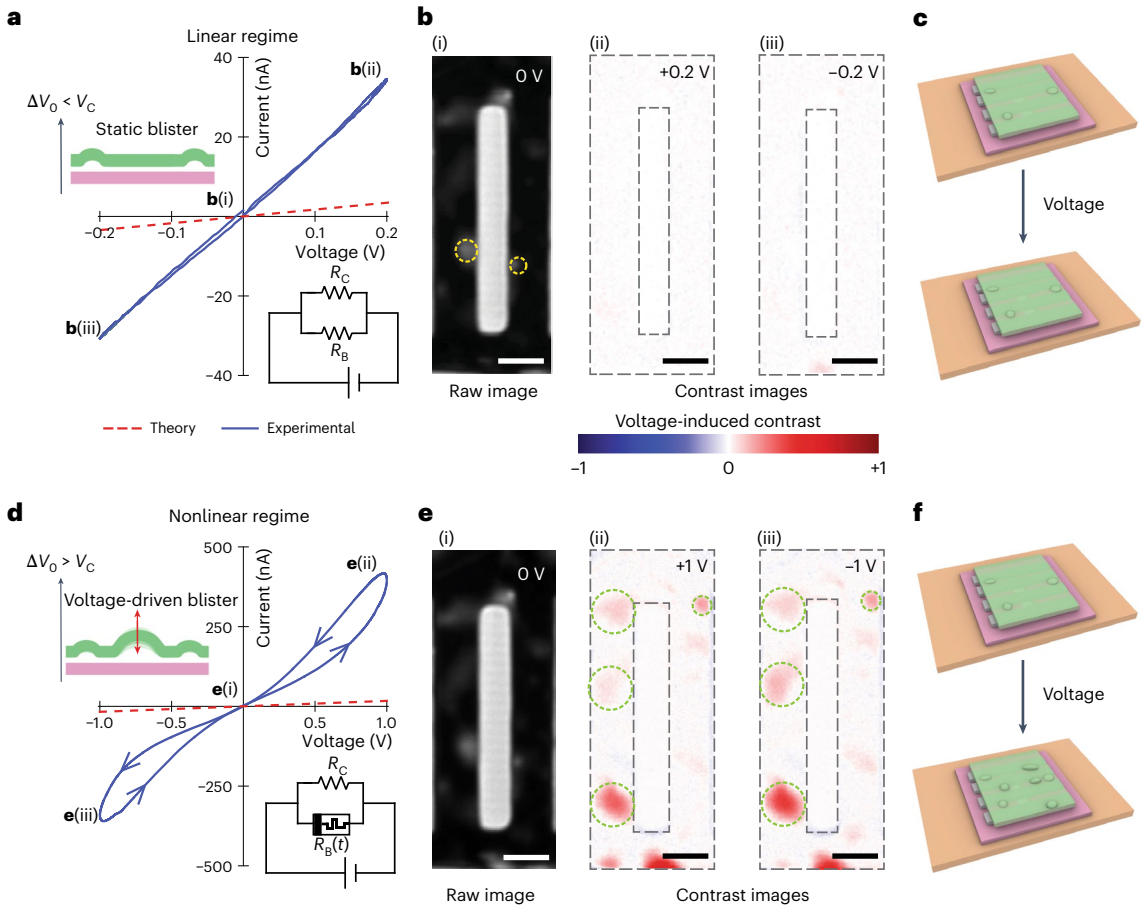


Fig. 2 | Origin of memory in 2D nanochannels. a,**d**, *I*–*V* characteristics of device 1 (five-layer graphene spacer) in 1 M KCl for a driving voltage $\Delta V(t) = \Delta V_0 \sin(2\pi ft)$ at a frequency $f = 100$ mHz showing a transition from a linear ion transport phenomenon to memristive hysteresis. **a**, *I*–*V* characteristic for $\Delta V_0 = 0.2$ V showing a linear ion transport regime with no hysteretic behaviour in the curve. **b**, A corresponding snapshot of the raw image at 0 V (i) and VIC images captured at +0.2 V (ii) and −0.2 V (iii) show no evidence of deformations or blister formation within the nanochannel. **c**, Schematic image of the absence of evolution of blisters in a nanochannel device under applied voltage $\Delta V_0 = 0.2$ V. **d**, *I*–*V* characteristic for $\Delta V_0 = 1$ V showing a nonlinear ion transport regime with hysteretic behaviour. Arrows indicate the hysteresis loop direction. **e**, A corresponding snapshot of the raw image at 0 V (i) and VIC images showing evidence of deformations (circled in green) at +1 V (ii) and −1 V (iii). **f**, Schematic image of the evolution of blisters in a nanochannel device under applied voltage $\Delta V_0 = 1$ V. Top left insets in both *I*–*V* plots (**a**,**d**): schematics of the device structure with blisters, corresponding to the conduction behaviour. The black upward arrow indicates the potential drop across the blister and the double-headed red arrow indicates the voltage-dependent deformation. Bottom right insets: the equivalent circuits, where R_C and R_B are the channel and blister resistances, respectively. In the nonlinear case, $R_B(t)$ is a memristor. The dashed red lines in both the *I*–*V* graphs represent the theoretical current obtained from the theoretical conductance, calculated on the basis of the device parameters. Scale bars, 5 μm. Supplementary Video 1 presents the full data in **d** and **e**.

traversed by light, where each interface contributes to reflection and propagation through each layer introduces a dephasing, which can be calculated through the transfer-matrix method (Supplementary Note 5). This enables retrieval of h_B, which is the only parameter susceptible to evolution under the application of a voltage. Our calculations showed that for parameters used in this work the contrast increases from zero to positive values on blister formation (Fig. 1e). The layered structure was determined by optical contrast on the exfoliation wafer, with thicknesses known within a ~10-nm-wide window around target values, resulting in small contrast changes highlighted in Fig. 1e. Thus, we primarily report the model-independent contrast Ψ throughout this work, treating converted heights as order-of-magnitude estimates.

Ion transport nonlinearities originate from voltage-driven blister formation

We measured nonlinear current–voltage (*I*–*V*) characteristics as previously reported in similar devices[13,28], which we investigated with our correlative approach. Varying the sinusoidal voltage amplitude ΔV_0 at high salt concentration (1 M KCl) from 0.05 V to 1 V (Supplementary Fig. 7), we observed linear ion conduction at low voltage amplitude (Fig. 2a, $\Delta V_0 < V_c \approx 0.2$ V). Although the *I*–*V* characteristic is linear, the measured conductance is several times higher than the expected theoretical value (Fig. 1c). This is evident from the raw image Fig. 2b(i), where areas with different contrast are circled in yellow, identifying liquid-filled blisters. This previously overlooked imperfect adhesion could result in an underestimation of the effective channel cross-section in addition to the previously proposed contribution of interfacial hydroxide ions[29]. In this regime of linear conduction, no significant VIC is observed at either positive or negative voltages (Fig. 2b(ii),(iii)): blisters circled in yellow in Fig. 2b(i) are not voltage responsive (Fig. 2a inset). For larger applied voltages $\Delta V_0 > V_c$, we observed the onset of nonlinearities including memristive hysteresis (Fig. 2d), coinciding with the appearance of blisters at high absolute value of the voltage (green circles, Fig. 2e). Blister formation and/or enlargement inside the nanochannel area have the effect of temporarily increasing the device's cross-section, thereby increasing its conductance. This shows the electromechanical origin of the nonlinearity of the *I*–*V* characteristic. Crucially, the strictly linear response observed in the absence of dynamic blister

https://doi.org/10.1038/s41563-026-02775-4

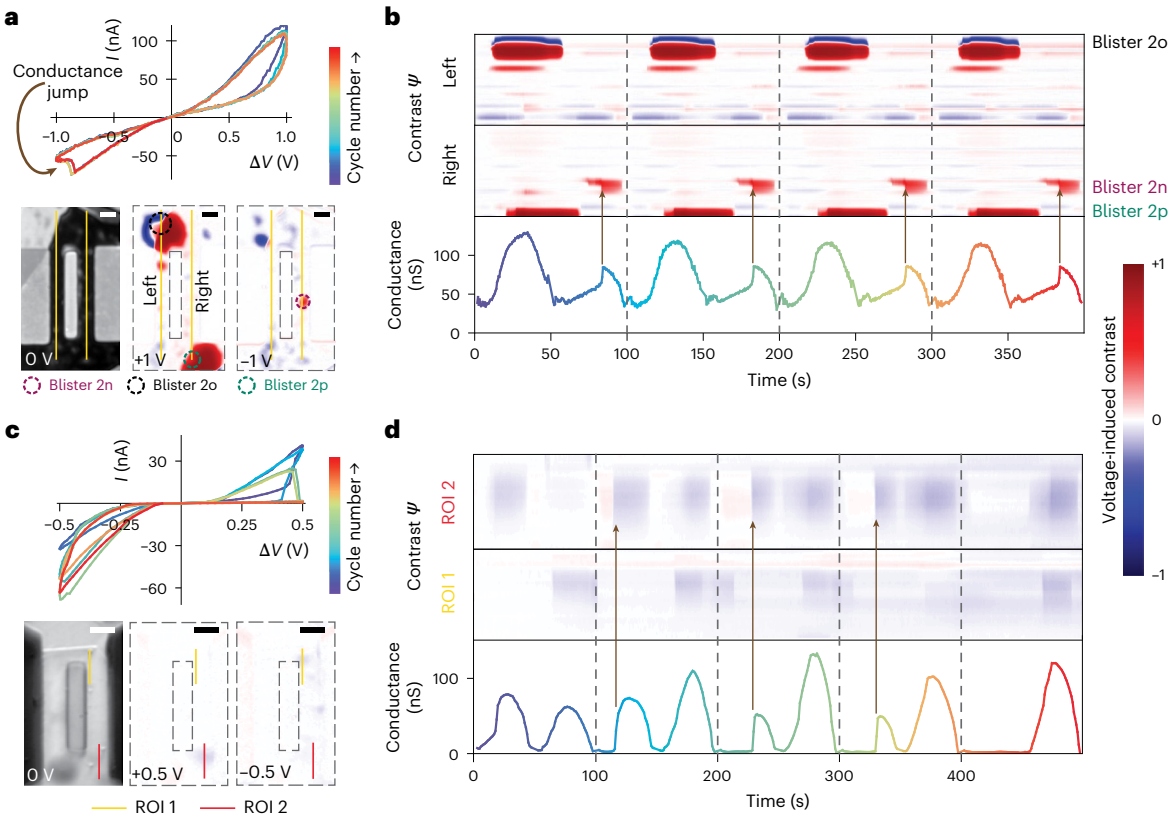


Fig. 3 | Spatiotemporal analysis of conductance jumps and device stochastic evolution. a, Repeated *I*–*V* characteristics of device 2 (1 M KCl at a frequency $f = 10$ mHz) exhibiting a conductance jump around −0.7 V, and the corresponding raw image at 0 V and VIC images at ±1 V. **b**, VIC kymographs extracted along the lines labelled 'Left' and 'Right' in **a**, correlated with the conductance–time trace. While many voltage-responsive blisters are present, this analysis enables pinpointing of which blister opens the ionic path creating the conductance jump effect. **c**, Consecutive *I*–*V* characteristics and corresponding images of the first cycle for device 6, which includes a gold patch. The device exhibited hysteresis that evolved over cycles, as shown by the non-overlapping characteristics. **d**, VIC kymographs extracted along the yellow and red lines in **c**, showing the two voltage-responsive regions of the device. Both react to voltage in a stochastic manner, and together ROI 1 and ROI 2 account for all conductance variations observed in the time trace. The time colour codes of the *I*–*V* characteristics match the respective conductance time traces. The dashed lines in panels **b** and **d** indicate individual voltage cycles. Scale bars, 5 µm.

deformation (Fig. 2a) implies that active structural evolution is required for hysteresis (Supplementary Discussion).

Blister stochasticity explains ion transport anomalies and evolution

We applied our correlative approach to devices exhibiting *I*–*V* characteristics of different shapes, to investigate their distinctive features and localize the device regions responsible for the nonlinear response. Device 2 (Fig. 3a) exhibits a repeatable conductance jump (+50% over <1 s) around −0.7 V. VIC kymographs (Fig. 3b) trace this jump precisely to a structural change at blister 2n (brown arrows). This directly links local confinement changes to macroscopic device conductance, explaining 2D slit conductance jumps not captured by ion-specific phenomenological models. Additionally, the top left blister 2o has a negative VIC for the part that is not covered by the top layer, in accordance with calculations (Supplementary Fig. 5). Blisters may thus not only form between top and bottom layers but also between the bottom layer and the SiN_x membrane (Supplementary Fig. 8a), contributing to the observed conductance changes alongside blister 2p.

We also examined irreversible conductance evolution in device 6 (Fig. 3c), whose four cycles produce non-overlapping *I*–*V* characteristics (its large ON/OFF ratio of 50 highlights the neuromorphic potential of 2D slit blistering). VIC images revealed two voltage-sensitive regions ROI 1 and ROI 2 corresponding to the formation of blisters with a negative VIC, a response expected for the gold-patched nanochannel device geometry; negative VIC upon blister formation is expected for this particular device geometry, used in previous studies[13,14,28] (Supplementary Fig. 4). Note that the irreversible changes reported here were also observed in devices without this gold patch, and conversely gold-patch devices were not all prone to irreversible evolution in similar experimental conditions. Kymograph analysis (Fig. 3d) cleanly decomposes the device's complex, stochastic conductance trace into the discrete contributions of ROI 1 and ROI 2. In particular, when the blister in ROI 1 skips the fourth cycle, the conductance does not increase as for the first three cycles in the corresponding time window. Likewise, the abrupt conductance jumps identified with the brown arrows coincide precisely with abrupt VIC jumps of ROI 2. For gold-patch devices (Fig. 3c,d and Supplementary Fig. 8c), we found VIC values not exceeding 0.1 in absolute value, which indicates deformations under ~5 nm (Supplementary Fig. 4).

By comparing the two aforementioned devices, we conclude that a highly repeatable *I*–*V* curve is the consequence of a stable blister landscape. This voltage-driven blistering phenomenology revealed through our correlative measurement approach thus explains the conduction anomalies in devices 1–3 and the other 11 devices reported in this work.

To further characterize these deformations, we next examined how individual blisters respond to the polarity of the applied voltage. This directionality analysis revealed two distinct response types: blisters that expand at both voltage polarities (device 1, Fig. 4a, shown in Supplementary Video 1) and blisters that expand only under one polarity (device 2, Fig. 4b, shown in Supplementary Video 2). This distinction already points to different underlying driving forces, which we explore

https://doi.org/10.1038/s41563-026-02775-4

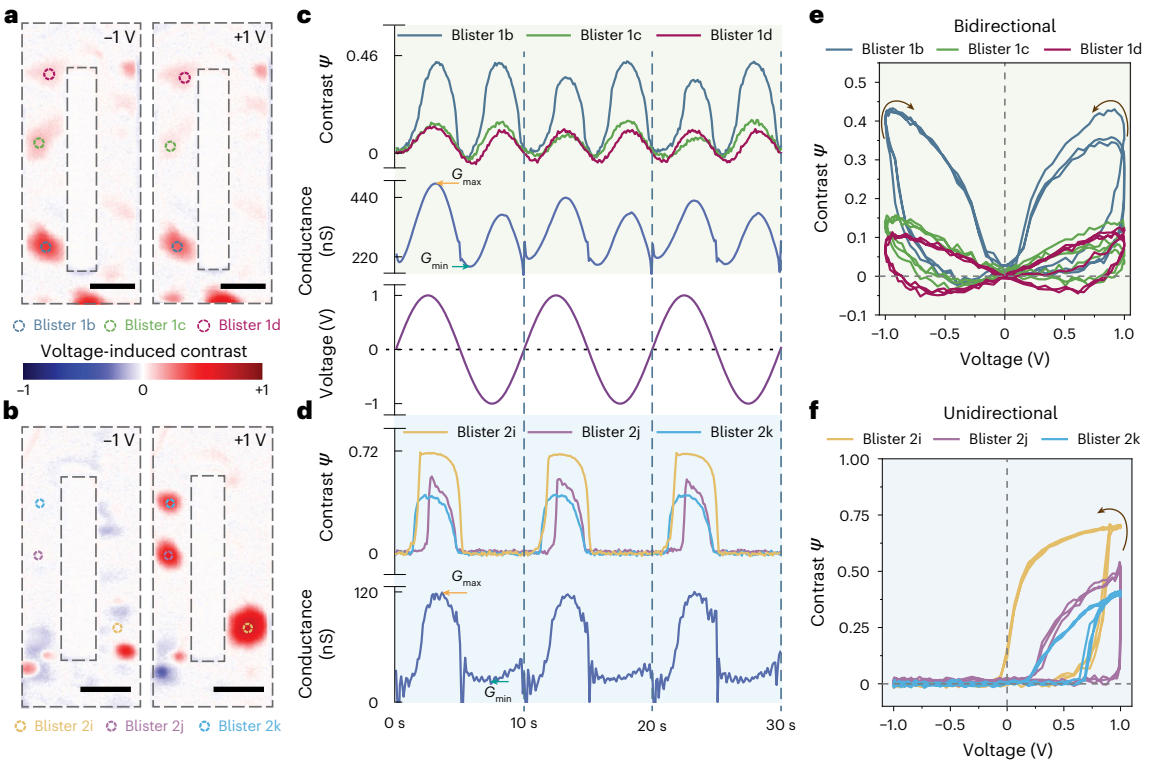


Fig. 4 | Imaging reveals two types of voltage-responsive blister. a, VIC images of device 1 at ±1 V (1 M KCl at f = 100 mHz), showing near-symmetric deformations for positive and negative voltage. **b**, VIC images of device 2 at ±1 V (1 M KCl at f = 100 mHz), showing unidirectional deformations for positive voltage only. **c**, VIC time traces of device 1 taken at the ROIs highlighted in **a**, and the conductance trace, which increases regardless of the sign of the voltage forcing. **d**, VIC time traces of device 2 taken at the ROIs highlighted in **b**, and the conductance trace, which increases only at positive voltages. **e**, The Ψ–V characteristics of the ROIs, showing a bidirectional pattern. **f**, The Ψ–V characteristics of the ROIs, showing a unidirectional positive pattern. The dashed vertical lines in **c** and **d** indicate individual voltage cycles. Scale bars, 5 µm.

more quantitatively in the following sections (corresponding I–V in Supplementary Fig. 9). The VIC time traces of the blisters circled in Fig. 4a are presented in Fig. 4c. We find that, just like the conductance time trace, all three VIC traces consistently increase at both positive and negative voltages. In contrast, for device 2 the VIC and conductance increases occur only at positive voltages while no blister forms at negative voltages (Fig. 4d). This directionality analysis can be visualized through contrast–voltage (Ψ–V) characteristics: for device 1, all three blisters had bidirectional Ψ–V characteristics (Fig. 4e), while all three blisters of device 2 had unidirectional positive Ψ–V characteristics (Fig. 4f). Supplementary Fig. 10 shows the conductance versus VIC for bidirectional (device 1) and unidirectional (device 2) hysteresis, respectively. Additionally, unidirectional blisters of Fig. 4f exhibit different threshold voltages for blister formation: blister 2i forms at near-zero voltage, while blister 2j and blister 2k form around +0.25 V. Once this voltage threshold is overcome, the blister VIC evolves progressively to a maximum value that corresponds to the maximum blister height of the order of 5–25 nm according to Fig. 1e.

While these two devices exhibit uniform blister directionality, we also observed hybrid cases featuring a mixture of bidirectional and unidirectional blisters (Supplementary Figs. 6 and 17), which yield complex asymmetrical I–V characteristics. This phenomenological diversity extends to the dynamics and retention of these electromechanical deformations. Frequency-dependent measurements revealed that both the macroscopic I–V hysteresis and individual blister loop areas decrease with increasing driving frequency (Supplementary Figs. 12–15). Crucially, by monitoring the structural state of the channels at the zero-voltage crossing during these sweeps, we uncovered the physical origin of memory retention. While the majority of deformations are purely volatile and collapse fully at 0 V, particularly at higher driving frequencies (Supplementary Fig. 17), a specific subset of blisters sustains a non-zero structural deformation even after the bias is removed (Supplementary Fig. 16). These non-volatile states emerge primarily at lower frequencies for device 2 (10–30 mHz), where unidirectional blisters have sufficient time to grow and reach the large-scale deformations required for memory retention (Supplementary Fig. 17a,b).

To quantitatively characterize the electromechanical landscape underlying ionic memory, we systematically analysed voltage-induced blister dynamics across multiple devices ($N = 9$). Figure 5a illustrates the extraction of two descriptors from correlative measurements from the time traces of the VIC $\Psi(t)$ and the normalized conductance variation $\delta G(t) = (G(t) - G_{min})/(G_{max} - G_{min})$. First, to quantify the directionality of blister expansion under each voltage polarity, we compute the symmetry ratio $S = A_{small}/A_{large}$, where A_{small} and A_{large} are the areas under the blister's VIC trace $\Psi(t)$ integrated over each half-cycle of the applied voltage. This ratio measures whether blister expansion is bidirectional ($S \approx 1$) or unidirectional ($S \ll 1$). Second, the contrast–conductance correlation $C = \langle \delta G(t) \times \Psi(t) \rangle$ quantifies how strongly blister VIC covaries with normalized conductance. Applying these metrics to all blisters ($N = 50$ across nine devices), we show in Fig. 5b that the symmetry ratio clusters cleanly into two populations: unidirectional blisters and bidirectional blisters. By contrast, the correlation C displays a broader spread, reflecting that the impact of a single blister on conductance depends not only on its underlying mechanism, but also on its location within the channel and on the presence of other active blisters in the same device. High C values nevertheless identify instances where specific blister dynamics dominate conductance, consolidating the causal link between local electromechanical activity and memristive ion transport. Finally, mapping the spatial distribution of blisters across devices (Fig. 5c) reveals their stochastic nature: they nucleate

https://doi.org/10.1038/s41563-026-02775-4

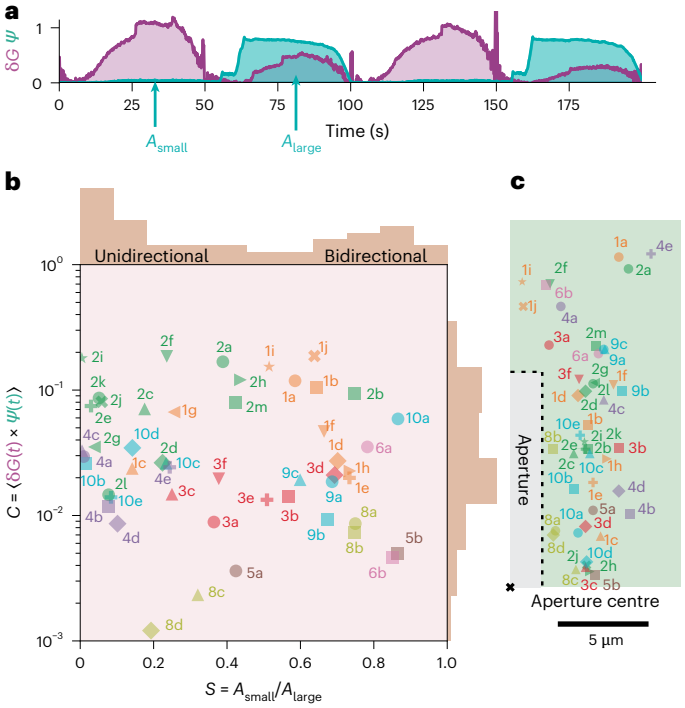


Fig. 5 | Statistical analysis of blister dynamics and correlation with ion transport. a, Example trace of δG and Ψ for blister 2g, illustrating the definition of $S = A_{small}/A_{large}$ and the time-averaged overlap between VIC and conductance $C = \langle \delta G \times \Psi \rangle$. **b**, Scatter plot of C versus S for all blisters analysed in hBN devices ($N = 50$ blisters from nine devices). Two populations emerge: unidirectional ($S \ll 1$) and bidirectional ($S \approx 1$). **c**, Spatial distribution of blister positions relative to the aperture centre, overlaid for all devices. All locations were collapsed into one quadrant owing to the device's double axial symmetry. Blister coordinates are given relative to the black cross at the bottom left, indicating the aperture centre. See Supplementary Fig. 23 for the full C–S plot with error bars and exhaustive blister positions.

unpredictably throughout the active region without globally preferred sites. Bidirectional blisters are consistently found on sites contributing to the ion path, whereas this is not strictly required for unidirectional ones (Supplementary Fig. 23c). This spatial and morphological stochasticity explains the strong device-to-device variability and temporal evolution (Supplementary Figs. 18–20) in nominally identical channels, highlighting stochastic blistering as the unifying origin of the diverse memristive behaviours observed in 2D nanofluidics.

Theoretical modelling of the observed deformations

Having shown that ion conduction nonlinearities arise from blister (de) formation between the layers of the 2D nanochannels, we modelled this system to identify the source of these electromechanical effects. We first estimated the pressure required to produce the observed deformations by deriving the full energy balance of blister formation[30], including the adhesion energy Γ of hBN on the spacer, the elastic (stretching[31]) energy of the deformed layer and the work of the pressure force (Fig. 6a; details in Supplementary Note 7.1). Larger blisters are energetically favoured, but in practice their size is limited by the channel region, giving the experimentally observed radii $R \approx 1$–2.5 µm. The corresponding detachment pressure P_c needed to cross the adhesion barrier is given by

$$P_c \approx \frac{(2Y_{\parallel} t_L)^{1/4} (8\Gamma)^{3/4}}{3R} \tag{2}$$

where $Y_{\parallel}$ is the in-plane Young's modulus of hBN and t_L the thickness of the deformed layer. While symmetric hBN devices (devices 1–4) prevent us from localizing the blister interface, asymmetric designs clarify these locations. We confirmed blisters between top and bottom layers using opaque graphite bottom layer (devices 9, 10 and 14), and demonstrated the possibility of blistering between the bottom hBN layer and SiN_x substrate by imaging bare hBN flake on SiN_x in devices 12 and 13 (Supplementary Fig. 21). Once this threshold is crossed ($P > P_c$), adhesion no longer applies and blister height follows

$$h_B \approx \left(\frac{3PR^4}{2Y_{\parallel} t_L} \right)^{1/3}. \tag{3}$$

Experimental data correspond to typical nanofluidic pressures (~1 bar)[32,33], but attaining P_c requires a Γ two orders of magnitude below its maximal value on pristine hBN/graphene interfaces ($\Gamma_{max} = 150$ mJ m^{-2})[34]. This reduced adhesion could reflect nanometre-thin hydrocarbon films persisting on 2D surfaces even after annealing, known to lower interfacial adhesion and to be remodelled in fluidic environments[35–37]. Consistent with this, our annealed device (Supplementary Fig. 11a) still showed blistering, indicating that the controlling factor is not dry-state cleanliness, but rather how the interface evolves in solution under applied bias. Adhesion is nevertheless crucial, as it may explain the memory effect (Fig. 6b): the barrier must be overcome by a growing blister but does not apply to a receding one, which simply follows equation (3). We thus predict that blister height, and hence conductance, exhibits hysteresis during a voltage cycle, smoothed both by disorder in the adhesion landscape and by the dynamics of blister filling. We further predict this hydrodynamic effect to suppress the memory at frequencies above ~100 mHz, as the blister no longer has time to grow (Supplementary Note 7.1.5). Regarding the source of the detachment pressure, we identified two phenomena that can supply it, yielding either a bidirectional or unidirectional voltage response.

In the first model, we considered the in-plane electric field along the channel of uniform negative surface charge Σ (Fig. 6c). The Dukhin number $\mathrm{Du} = |\Sigma|/ec_0h \approx 0.2$ is modest at 1 M but increases at lower concentrations, and its coupling with the strong potential drop $e\Delta V/k_BT \approx 40$ for $\Delta V = 1$ V suffices to generate significant concentration polarization (Supplementary Note 7.2)[38]. Indeed, cations dragged along the channel by the field produce a salt overconcentration on one side and depletion on the other. Coupling ionic transport to the electric field set by the local ionic resistivity, we predict the salt concentration profile (Fig. 6d), whose average always exceeds the equilibrium concentration. This extra salt generates an average osmotic pressure between channel and reservoir, pushing the top layer upwards:

$$P_{osm} = \frac{\mathrm{Du}}{1 + \mathrm{Du}} \frac{|\Sigma| e \Delta V^2}{96 h k_B T}. \tag{4}$$

With $\Sigma \approx -30$ mC m^{-2}, $h \approx 3$ nm and $c_0 = 1$ M, this predicts osmotic pressures up to 4 bar (refs. 28,39,40). Since the overpressure occurs regardless of the sign of ΔV, this model yields bidirectional memristors, whose height over a voltage cycle (Fig. 6e) compares well with those of experimentally observed blisters (orange). Substituting equation (4) into equation (3) further predicts $h_B \propto \Delta V^{2/3}$ once adhesion is overcome, consistent with experimental data (Supplementary Fig. 24a).

In the second model, we considered the out-of-plane electric field ($E_\perp$). Due to the device geometry, field lines not only run along the channel but also cross the top and bottom layers (Fig. 6f). The surface charges at the interfaces are thus pulled in the normal direction, for which they are weakly screened ($\epsilon^{\perp}_s \approx 2.1$), unlike their counter-charges surrounded by water ($\epsilon_w \approx 80$) (Fig. 6g)[41]. Under applied voltage, the surface charge then induces an electrostatic pressure on the wall (Supplementary Note 7.3):

https://doi.org/10.1038/s41563-026-02775-4

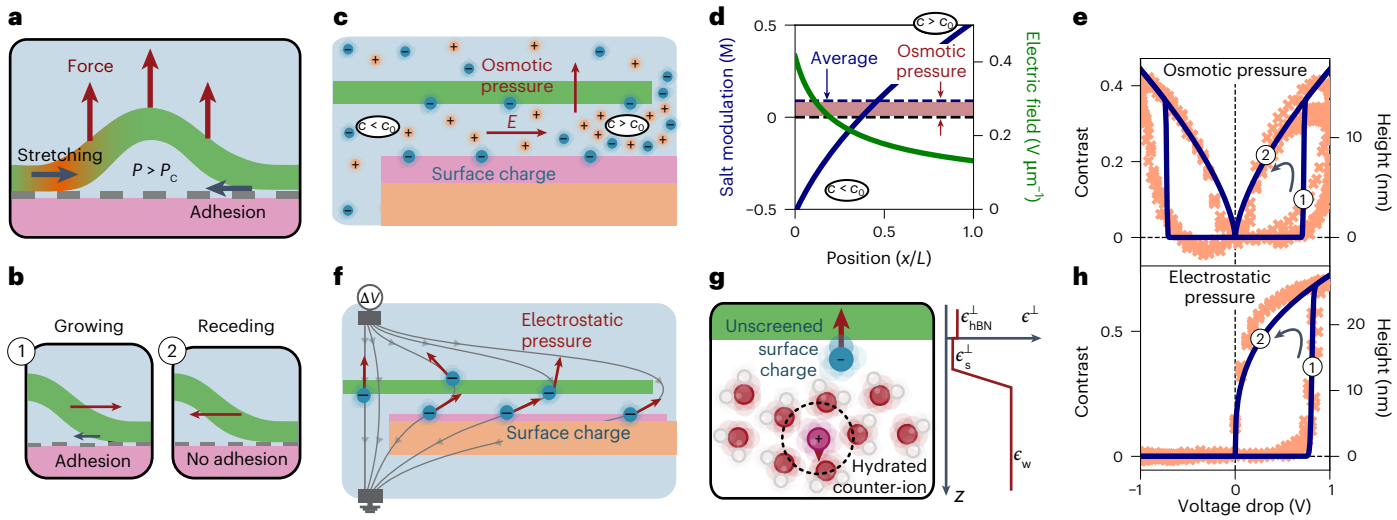


Fig. 6 | Mechanism of voltage-induced blister (de)formation. a, Sketch of a blister, pulled by an upward pressure-driven force when pressure overcomes the stretch and the adhesion on the spacers, defining P_c. **b**, Sketch of the growing and receding of a blister. The presence of the adhesion energy barrier while the blisters grow but not when they decrease induces a mechanical hysteresis leading to ion transport memory. **c**, Sketch of the nanochannel in the presence of an electric field: the transport of the excess of cations due to the surface charge generates a concentration polarization along the channel. **d**, Blue: the salt concentration modulation compared with the equilibrium concentration, $c(x)-c_0-|\Sigma|/h$, along the channel. The dashed line is the average salt concentration excess, which leads to the osmotic pressure. Green: the corresponding electric field along the channel, modulated by the local ionic resistivity. x/L represents the normalized position along the channel. **e**, Prediction of blister height and the corresponding contrast as a function of the voltage in a cycle. The arrow indicates the direction of the cycle and the numbers refer to **b**. The orange crosses correspond to the experimental data of blister 1b (Fig. 4), for which we used an effective $R = 1\,\mu m$ and fitted an effective $\Gamma = 1.5\,mJ\,m^{-2}$ and $\Sigma = -16\,mC\,m^{-2}$. **f**, Sketch of the device with electric field lines crossing the top and bottom layers and pulling surface charges. **g**, Zoom on a surface charge and its counter-charge. While the counter-charge is surrounded by water molecules efficiently screening the ion (ϵ_w), the surface charge is only weakly screened in the normal direction ($\epsilon^{\perp}_s \ll \epsilon_w$), resulting in a stronger electrostatic force acting on surface charges than on counter-ions. **h**, Prediction of blister height and the corresponding contrast as a function of the voltage in a cycle. The arrow indicates the direction of the cycle and the numbers refer to **b**. The orange crosses correspond to the experimental data of blister 2i (Fig. 4), for which we used an effective $R = 1.5\,\mu m$ and fitted an effective $\Gamma = 4.1\,mJ\,m^{-2}$ and $\Sigma = -22\,mC\,m^{-2}$.

$$P_{elec} = 2\Sigma E_{\perp} \approx -\frac{2\Sigma\,\Delta V}{t_L \epsilon_{\perp s}}. \quad (5)$$

With $\Sigma = -30\,mC\,m^{-2}$, this predicts electrostatic pressures up to 3 bar. Here, the force direction depends on the sign of ΔV: generating a blister on the top layer requires an upward force, corresponding to positive ΔV for a negative surface charge. As shown in Fig. 6h, this electrostatic pressure thus produces positive unidirectional memristors, again comparing well with experimentally observed blisters (orange). In this model, channel height instead scales as $h_B \propto \Delta V^{4/3}$, also consistent with experimental data (Supplementary Fig. 24a).

Independent of the mechanism, our models predict a strong sensitivity to surface charge, which is corroborated experimentally by varying salt concentration (Supplementary Fig. 22)[29,40]. While previous work[21] reported the formation of micrometre-scale blisters (that can be rationalized as unidirectional positive), we observe here much smaller and more diverse deformations in 2D nanochannels. The majority of unidirectional blisters form at positive voltages as in Fig. 4f, but we also found occurrences of negative unidirectional blisters such as the one presented in Fig. 5a and Supplementary Fig. 11a. We attribute this variability to the complexity of the layered structure and the possible local variations in the surface charge landscape. This points to a rich and device-dependent phenomenology that has probably been overlooked on other nanofluidic platforms. These results demonstrate that, to fully capture the physics of nanofluidic transport, we must consider not only the forces acting on the confined molecules but also those exerted on the confining walls.

Outlook and conclusion

In summary, voltage-induced mechanical blistering drives current–voltage hysteresis and ionic memory in 2D nanochannels. Physical deformation acts as the primary state variable for the observed memory, overriding purely ionic effects (Supplementary Discussion). The stochastic nature of these deformations explains device variability and evolution, and probably extends to other nanofluidic architectures. Two electromechanical pathways generate sufficient stress to overcome van der Waals adhesion: osmotic pressure from concentration polarization and electrostatic forces on surface charges. The assumption of static confining walls does not hold at high voltages, revealing an intrinsic coupling between mechanics and transport that parallels the conformational gating of biological ion channels[42]. By fully accounting for these behaviours, our approach provides the basis for overcoming variability challenges, a necessary step towards reliable nanofluidic technologies.

By rationalizing the behaviour of all measured devices, our correlative approach calls for the widespread use of operando imaging to understand nonlinear nanoscale ion transport and reassess previous conclusions. Because purely ionic memory mechanisms would induce minute refractive-index variations (<1%), resulting signals would probably fall below our technique's detection limit, contrasting with its pronounced sensitivity to structural deformations. To address this, complementary operando imaging approaches could be employed in systems lacking mechanical distortions. For ultrasmall architectures such as nanotubes or biological nanopores, single-molecule super-resolution microscopy is a promising strategy. Beyond imaging, controlling nanofluidic blisters via mechanics and interfacial chemistry provides concrete design principles for ionic memory (for example, by deterministic placement of nanofabricated low-adhesion zones[43,44]). On this basis, high-performance nanofluidic synapses integrated into large-scale liquid circuits become a realistic prospect for advanced ionic computing.

Online content

Any methods, additional references, Nature Portfolio reporting summaries, source data, extended data, supplementary information, acknowledgements, peer review information; details of author contributions and competing interests; and statements of data and code availability are available at https://doi.org/10.1038/s41563-026-02775-4.

References

1. Emmerich, T. et al. Nanofluidics. *Nat. Rev. Methods Primers* **4**, 69 (2024).
2. Kavokine, N., Netz, R. R. & Bocquet, L. Fluids at the nanoscale: from continuum to subcontinuum transport. *Annu. Rev. Fluid Mech.* **53**, 377–410 (2021).
3. Feng, J. et al. Observation of ionic Coulomb blockade in nanopores. *Nat. Mater.* **15**, 850–855 (2016).
4. Karnik, R., Duan, C., Castelino, K., Daiguji, H. & Majumdar, A. Rectification of ionic current in a nanofluidic diode. *Nano Lett.* **7**, 547–551 (2007).
5. Vlassiouk, I. & Siwy, Z. S. Nanofluidic diode. *Nano Lett.* **7**, 552–556 (2007).
6. Ali, M., Ramirez, P., Mafé, S., Neumann, R. & Ensinger, W. A pH-tunable nanofluidic diode with a broad range of rectifying properties. *ACS Nano* **3**, 603–608 (2009).
7. Rabinowitz, J. et al. Nanobubble-controlled nanofluidic transport. *Sci. Adv.* **6**, eabd0126 (2020).
8. Davis, S. J. et al. Pressure-induced enlargement and ionic current rectification in symmetric nanopores. *Nano Lett.* **20**, 8089–8095 (2020).
9. Xiong, T. et al. Neuromorphic functions with a polyelectrolyte-confined fluidic memristor. *Science* **379**, 156–161 (2023).
10. Zhou, X. et al. Nanofluidic memristor based on the elastic deformation of nanopores with nanoparticle adsorption. *Natl Sci. Rev.* **11**, nwad216 (2024).
11. Mayer, S. F. et al. Lumen charge governs gated ion transport in β-barrel nanopores. *Nat. Nanotechnol.* **21**, 116–124 (2026).
12. Liu, K. et al. Resistance-restorable nanofluidic memristor and neuromorphic chip. *Nano Lett.* **25**, 6530–6538 (2025).
13. Robin, P. et al. Long-term memory and synapse-like dynamics in two-dimensional nanofluidic channels. *Science* **379**, 161–167 (2023).
14. Ismail, A. et al. Programmable memristors with two-dimensional nanofluidic channels. *Nat. Commun.* **16**, 7008 (2025).
15. Xu, G. et al. Nanofluidic ionic memristors. *ACS Nano* **18**, 19423–19442 (2024).
16. Law, C. S. et al. Recent advances in fluidic neuromorphic computing. *Appl. Phys. Rev.* **12**, 021309 (2025).
17. Zhang, M., Xu, G., Zhang, H. & Xiao, K. Nanofluidic volatile threshold switching ionic memristor: a perspective. *ACS Nano* **19**, 10589–10598 (2025).
18. Bocquet, L. Nanofluidics coming of age. *Nat. Mater.* **19**, 254–256 (2020).
19. Ronceray, N. et al. Liquid-activated quantum emission from pristine hexagonal boron nitride for nanofluidic sensing. *Nat. Mater.* **22**, 1236–1242 (2023).
20. Loessberg-Zahl, J. et al. Exploring voltage mediated delamination of suspended 2D materials as a cause of commonly observed breakdown. *J. Phys. Chem. C* **124**, 430–435 (2020).
21. Emmerich, T. et al. Nanofluidic logic with mechano–ionic memristive switches. *Nat. Electron.* **7**, 271–278 (2024).
22. Robin, P., Kavokine, N. & Bocquet, L. Modeling of emergent memory and voltage spiking in ionic transport through angstrom-scale slits. *Science* **373**, 687–691 (2021).
23. Toquer, D., Bocquet, L. & Robin, P. Ionic association and Wien effect in 2D confined electrolytes. *J. Chem. Phys.* **162**, 064703 (2025).
24. Ismail, A. et al. When does nanofluidic memory disappear? Understanding and reinstating memristive behavior of ionic liquids in two-dimensional nanochannels. *Faraday Discuss.* **266**, 446–463 https://doi.org/10.1039/D5FD00142K (2026).
25. Radha, B. et al. Molecular transport through capillaries made with atomic-scale precision. *Nature* **538**, 222–225 (2016).
26. Bhardwaj, A. et al. Fabrication of angstrom-scale two-dimensional channels for mass transport. *Nat. Protoc.* **19**, 240–280 (2024).
27. Ronceray, N. et al. Elastocapillarity-driven 2D nano-switches enable zeptoliter-scale liquid encapsulation. *Nat. Commun.* **15**, 185 (2024).
28. Esfandiar, A. et al. Size effect in ion transport through angstrom-scale slits. *Science* **358**, 511–513 (2017).
29. Emmerich, T. et al. Enhanced nanofluidic transport in activated carbon nanoconduits. *Nat. Mater.* **21**, 696–702 (2022).
30. Chopin, J., Vella, D. & Boudaoud, A. The liquid blister test. *Proc. R. Soc. A* **464**, 2887–2906 (2008).
31. Wang, G. et al. Bending of multilayer van der Waals materials. *Phys. Rev. Lett.* **123**, 116101 (2019).
32. Marcotte, A., Mouterde, T., Niguès, A., Siria, A. & Bocquet, L. Mechanically activated ionic transport across single-digit carbon nanotubes. *Nat. Mater.* **19**, 1057–1061 (2020).
33. Marbach, S. & Bocquet, L. Osmosis, from molecular insights to large-scale applications. *Chem. Soc. Rev.* **48**, 3102–3144 (2019).
34. Sanchez, D. A. et al. Mechanics of spontaneously formed nanoblisters trapped by transferred 2D crystals. *Proc. Natl Acad. Sci. USA* **115**, 7884–7889 (2018).
35. Kim, Y., Herlinger, P., Taniguchi, T., Watanabe, K. & Smet, J. H. Reliable post processing improvement of van der Waals heterostructures. *ACS Nano* **13**, 14182–14190 (2019).
36. Haigh, S. J. et al. Cross-sectional imaging of individual layers and buried interfaces of graphene-based heterostructures and superlattices. *Nat. Mater.* **11**, 764–767 (2012).
37. Rokni, H. & Lu, W. Direct measurements of interfacial adhesion in 2D materials and van der Waals heterostructures in ambient air. *Nat. Commun.* **11**, 5607 (2020).
38. Kim, S. J., Wang, Y.-C., Lee, J. H., Jang, H. & Han, J. Concentration polarization and nonlinear electrokinetic flow near a nanofluidic channel. *Phys. Rev. Lett.* **99**, 044501 (2007).
39. Wang, Y. et al. Spontaneous surface charging and Janus nature of the hexagonal boron nitride–water interface. *J. Am. Chem. Soc.* **147**, 30107–30116 (2025).
40. Secchi, E., Niguès, A., Jubin, L., Siria, A. & Bocquet, L. Scaling behavior for ionic transport and its fluctuations in individual carbon nanotubes. *Phys. Rev. Lett.* **116**, 154501 (2016).
41. Fumagalli, L. et al. Anomalously low dielectric constant of confined water. *Science* **360**, 1339–1342 (2018).
42. Hille, B. Ionic channels in excitable membranes. Current problems and biophysical approaches. *Biophys. J.* **22**, 283–294 (1978).
43. Schweizer, P. et al. Mechanical cleaning of graphene using in situ electron microscopy. *Nat. Commun.* **11**, 1743 (2020).
44. Jia, Y. et al. Toward high carrier mobility and low contact resistance: laser cleaning of PMMA residues on graphene surfaces. *Nano-Micro Lett.* **8**, 336–346 (2016).
45. Saurav, K. V. et al. Dataset of 'Direct imaging elucidates ionic memory in two-dimensional nanochannels'. *figshare* https://doi.org/10.6084/m9.figshare.33269229 (2026).

Publisher's note Springer Nature remains neutral with regard to jurisdictional claims in published maps and institutional affiliations.

Open Access This article is licensed under a Creative Commons Attribution 4.0 International License, which permits use, sharing, adaptation, distribution and reproduction in any medium or format,

as long as you give appropriate credit to the original author(s) and the source, provide a link to the Creative Commons licence, and indicate if changes were made. The images or other third party material in this article are included in the article's Creative Commons licence, unless indicated otherwise in a credit line to the material. If material is not included in the article's Creative Commons licence and your intended use is not permitted by statutory regulation or exceeds the permitted use, you will need to obtain permission directly from the copyright holder. To view a copy of this licence, visit http://creativecommons.org/licenses/by/4.0/.

© The Author(s) 2026

Data availability

Source data related to this work are available via figshare at https://doi.org/10.6084/m9.figshare.33269229 (ref. 45).

Code availability

The Python script used for analysis can be accessed through the GitHub repository at https://github.com/nronce/operandoslit.

Acknowledgements

We acknowledge funding from the European Research Council (grants 101020445—2D-LIQUID to N.R. and A.R.), the Swiss National Science Foundation (grant TMPFP2-217134 to T.E.) and Swiss Government Excellence Scholarship to A.D.P.; B.R. acknowledges funding from the Royal Society University Research Fellowship renewal URF\R\231008, Philip Leverhulme Prize PLP-2021-262, European Union's H2020 Framework Programme ERC Grants (852674, AngstroCAP, and 101232407, ANGEL). B.R. and A.K. acknowledge EPSRC strategic equipment grant EP/W006502/1. A.K. acknowledges Royal Society International Exchanges grant IES\R3\243222. B.C. acknowledges support from the CFM Foundation and the NOMIS Foundation. N.R. acknowledges support from an EMBO fellowship (ALTF1237-2024).

Author contributions

B.R., A.R., T.E. and N.R. designed and directed the project. K.V.S. fabricated the nanochannel devices with inputs from B.R. and A.K. K.V.S. performed the operando measurements and their analysis, with input from N.R. and T.E. A.D.P. performed additional operando measurements. N.R. built the operando imaging microscope, and T.E. designed the fluidic cell. N.R. developed the Python script for image analysis, kymograph and statistical analysis. N.R. carried out transfer-matrix method calculations. B.C. developed the theoretical modelling with input from N.R.; K.V.S., N.R., T.E. and B.C. wrote the paper with inputs from A.R., A.K. and B.R. All authors contributed to the discussion.

Funding

Open access funding provided by EPFL Lausanne.

Competing interests

The authors declare no competing interests.

Additional information

Supplementary information The online version contains supplementary material available at https://doi.org/10.1038/s41563-026-02775-4.

Correspondence and requests for materials should be addressed to Theo Emmerich, Aleksandra Radenovic or Boya Radha.

Peer review information *Nature Materials* thanks the anonymous reviewers for their contribution to the peer review of this work.

Reprints and permissions information is available at www.nature.com/reprints.